Radiative opacities and configuration interaction effects of hot iron plasma using a detailed term accounting model

Fengtao Jin,[1] Jiaolong Zeng,[1,2] and Jianmin Yuan[1]
[1]*Department of Applied Physics, National University of Defense Technology, Changsha 410073, People's Republic of China*
[2]*National Astronomical Observatories, Chinese Academy of Sciences, Beijing 100012, People's Republic of China*
(Received 11 July 2003; published 11 December 2003)

We have calculated the radiative opacities of iron plasma in local thermodynamic equilibrium using a detailed term accounting model. The extensive atomic data are obtained by multiconfiguration Hartree-Fock (MCHF) method, with Breit-Pauli relativistic corrections. Extensive configuration interaction (CI) has been included based on *LS* coupling to obtain energy levels and the bound-bound transition cross sections. A detailed configuration accounting model is applied to evaluate the bound-free absorption cross sections. We simulate two experimental transmission spectra [G. Winhart *et al.*, Phys. Rev. E **53**, R1332 (1996); P. T. Springer *et al.*, J. Quant. Spectrosc. Radiat. Transf. **58**, 927 (1997)] to verify our calculation model, one is at a temperature of 22 eV and a density of 10^{-2} g/cm^3 and the other is at a temperature of 20 eV and a lower density of 10^{-4} g/cm^3. It is shown that the strong CI can effectively change the oscillator strengths in contrast to the single configuration HF method. For both of the two simulated transmission spectra good agreement is obtained between the present MCHF results and the experimental data. Spectrally resolved opacities and Planck and Rosseland mean opacities are also calculated. For the isothermal sequence of $T=20$ eV, when the density decreases from 10^{-2} to 10^{-5} g/cm^3, the linewidth also decreases so that the iron transition arrays show more discrete line structures and the linewidth becomes very important to the Rosseland mean opacity.

DOI: 10.1103/PhysRevE.68.066401 PACS number(s): 52.25.Os, 52.20.−j

I. INTRODUCTION

The research on the radiative opacities of hot dense plasma is first of interest in astrophysics and has been of particular importance in the study of stellar structure and evolution. Many theoretical models [1–7] and computer codes [1–3] have been developed such as the OPAL code [1] of the Lawrence Livermore National Laboratory and the LEDCOP code [2] of the Los Alamos National Laboratory. They have calculated the radiative opacities of low-*Z* and medium-*Z* elements and put them as a data server on internet. Also international collaborations such as the Opacity Project [8] and the Iron Project [9] have been organized to calculate accurately the enormous atomic data required by opacity. Among these works the opacity of the medium-*Z* iron plasma is of particular concern due to both the astrophysical needs and the technological challenge for theoretical models. Theoretical calculations of opacities are quite complex and usually need numerous approximations. Therefore different opacity models often lead to different results.

Experimental measurement of opacity is very important to verify the theoretical models. Many laboratory measurements of opacity had been done in the past decades. DaSilva *et al.* [10] measured the transmission of iron plasma at a temperature of 25 eV and a density of 0.008 g/cm^3 in the photon energy range of 50–120 eV. Winhart *et al.* [11,12] performed a measurement in the spectral range of 70–140 eV at a temperature of 22 eV and a density of 0.01 g/cm^3. Springer *et al.* [13,14] measured a spectroscopic opacity and also the Rosseland and Planck group mean opacities of iron plasma covering the spectral range of 80–100 eV at a temperature of 59 eV and a density of 0.0113 g/cm^3. In 1997, Springer *et al.* [15] measured another transmission spectrum of iron plasma near the critical region of stellar envelopes with the temperature of 20 eV and the density of 10^{-4} g/cm^3.

In this paper we performed a detailed term accounting (DTA) calculation of the radiative opacities of iron plasma with the multiconfiguration Hartree-Fock (MCHF) [16–18] method based on *LS* coupling, with Breit-Pauli relativistic corrections. Extensive configuration interaction (CI) calculations have been performed to obtain the massive atomic levels. Since the photoionization has a minor contribution to the total opacity for the cases we studied and requires much more efforts in the calculation, we applied a detailed configuration accounting (DCA) [19] model to deal with this part. We took the Kramers formula [20] to account for the free-free absorption and the Thomson scattering cross section for the photon scattering by the free electrons. Using this model, we calculated an isothermal sequence of iron opacities at a temperature of 20 eV. Detailed simulations for Winhart's [11] and Springer's [15] experiments have also been performed and good agreements have been obtained between the experimental and theoretical spectra.

II. METHOD OF CALCULATION

In the calculation of opacity, massive amounts of atomic data are required such as the atomic levels, level populations, line transitions, line shapes, photoionization cross sections, free-free absorption, and photon scattering by the free electrons. Plasma environment should also be considered.

A. MCHF method and population

In the MCHF method [16–18], the wave function of an atom containing many electrons is approximated by an expansion in a set of antisymmetric configuration state functions (CSF):

$$\Psi(\gamma LS)=\sum_{\alpha=1}^{M} c_\alpha \Phi(\gamma_\alpha LS), \tag{1}$$

where $\Psi(\gamma LS)$ is the atom wave function labeled by γLS, L is the total angular momentum, and S is the total spin, $\Phi(\gamma_\alpha LS)$ is a CSF with total angular momentum L and total spin S, γ_α represents the configuration and any quantum numbers other than LS that are needed for complete specification of the state. Each CSF is a vector coupled state of one-electron orbitals

$$\phi(r,\theta,\varphi,\sigma)=\frac{1}{r}P_{nl}(r)Y_{lm_l}(\theta,\varphi)\chi_{m_s}(\sigma), \tag{2}$$

where the spherical harmonics Y_{lm_l} and spinors χ_{m_s} are known. The radial functions $P_{nl}(r)$ are determined by the self-consistent field (SCF) method.

In case of the Breit-Pauli approximation, L and S are coupled to form a resultant angular momentum J. Now the atom wave function has the form

$$\Psi(\gamma LSJ)=\sum_{\alpha=1}^{M} c_\alpha \Phi(\gamma_\alpha L_\alpha S_\alpha J). \tag{3}$$

Therefore the wave function is a sum of configuration states for possibly different LS terms and the expansion coefficients are determined by the CI. The eigenvalue of state Ψ_i is given by

$$E_i=\langle\Psi_i|\hat{H}|\Psi_i\rangle \tag{4}$$

and the transition probability from state Ψ_i to Ψ_j is

$$f_{ij}=\frac{(E_j-E_i)}{3(2J+1)}|\langle\Psi_j\|\mathbf{P^{(1)}}\|\Psi_i\rangle|^2, \tag{5}$$

where f_{ij} is the oscillator strength and $\mathbf{P^{(1)}}$ is the electron dipole ($E1$) operator.

With the energy levels we can calculate the population distributions of different ionization stages in local thermodynamic equilibrium (LTE) plasma by the Saha equation [18,20]

$$\frac{N_{i+1}N_e}{N_i}=\frac{Z_{i+1}Z_e}{Z_i}\exp[-(\phi_i-\Delta\phi_i)/kT], \tag{6}$$

where N_i is the total population density of ion i, N_e is the number of free electrons per unit volume, ϕ_i is the ionization potential of ion i, $\Delta\phi_i$ is the ionization potential depression (IPD) caused by plasma environment, Z_i and Z_e are the partition functions for ion i and free electron. They are determined, respectively, by

$$Z_i=\sum_t g_{it}e^{-E_{it}/kT}, \tag{7}$$

$$Z_e=2\left(\frac{2\pi m_e kT}{h^2}\right)^{3/2}, \tag{8}$$

where E_{it} is the energy of level t of ion i above ground state and $g_{it}=2J+1$ is its degeneracy. Then the population of level t is determined by the Boltzmann distribution

$$N_{it}=g_{it}(N_i/Z_i)e^{-E_{it}/kT}. \tag{9}$$

The sum of Eq. (7) runs over all bound states of ion i and be truncated at the ionization threshold, which has been lowered by IPD. The Stewart-Pyatt [21] model is applied to calculate the IPDs in this paper:

$$\Delta\phi_i=\frac{\left[3(z^*+1)\dfrac{z_i e^2}{DkT}+1\right]^{2/3}-1}{2(z^*+1)}kT, \tag{10}$$

where D is the Debye length, z_i is the ion with ionization degree i, and z^* is the mean ionization degree.

B. Radiative opacity

The total opacity of a plasma is the combination of bound-bound, bound-free, free-free, and scattering processes. The bound-bound absorption coefficients for a photon with energy $h\nu$ are evaluated by

$$\mu_{bb}(h\nu)=\sum_i\left[\sum_{tt'} N_{it}\sigma_{itt'}(h\nu)\right], \tag{11}$$

where $\sigma_{itt'}$ is the cross section for the photoexcitation from term t to t' and evaluated by the formula

$$\sigma_{itt'}(h\nu)=\frac{\pi he^2}{m_e c}f_{itt'}S(h\nu)=109.71 f_{itt'}S(h\nu), \tag{12}$$

where $S(h\nu)$ is the line-shape function with $h\nu$ in eV and $\sigma_{itt'}$ in Mb. $f_{itt'}$ is the so-called oscillator strength from term t to t'. In our works we have considered both electron-impact broadening and Doppler broadening. The Doppler half width at half maximum (HWHM) [18] is given by

$$\Gamma_d=3.858\times10^{-5}(kT/A)^{1/2}(h\nu_0), \tag{13}$$

where A is the atomic weight of the ion in grams and kT, $h\nu_0$, and Γ are in eV. The electron-impact HWHM is expressed using a semiempirical formula [22,23]

$$\Gamma_l=N_e\frac{4\pi}{3}\frac{\hbar^3}{m^2e}\left(\frac{2m}{\pi kT}\right)^{1/2}\frac{\pi}{\sqrt{3}}\left(0.9-\frac{1.1}{z}\right)\sum_{j=i,f}\left(\frac{3n_j}{2z}\right)^2 \times(n_j^2-l_j^2-l_j-1), \tag{14}$$

where n_i, n_j, l_i, l_j are the principal and angular quantum numbers of the initial and final orbitals related with the transition. The line-shape function $S(h\nu)$ is applied with the Voigt profile where

$$S(h\nu)=\frac{\sqrt{\ln 2}}{\sqrt{\pi}\Gamma_d}H(a,v), \tag{15}$$

in which $H(a,v)$ is the Voigt function,

$$H(a,v)=\frac{a}{\pi}\int_{-\infty}^{+\infty}\frac{e^{-x^2}}{a^2+(v-x)^2}dx, \tag{16}$$

where $a=\sqrt{\ln 2}\Gamma_l/\Gamma_d$ and $v=\sqrt{\ln 2}(h\nu-h\nu_0)/\Gamma_d$.

Rose's DCA [19] method was applied to account for the bound-free contribution. The total photoionization cross section of ion i is a weighted sum running over all bound states that are explicitly considered:

$$\sigma_{bf}^{i}(h\nu)=\frac{\pi e^2}{m_e c}\sum_{\alpha} P_i(\alpha)\frac{df_{\alpha\to c}}{d(h\nu)}, \tag{17}$$

where $df_{\alpha\to c}/d\epsilon$ is the one-configuration photoionization oscillator density and $P_i(\alpha)$ is the relative probability of configuration α calculated by the Saha-Boltzmann equations. Then the total bound-free absorption coefficient of the plasma is

$$\mu_{bf}(h\nu)=\sum_{i} N_i\sigma_{bf}^{i}(h\nu). \tag{18}$$

Except for very low energy photons, the free-free contribution is very small compared with the bound-bound and bound-free absorptions, then the Kramers [19] cross section is used:

$$\sigma_{ff}(h\nu)=\frac{16\pi^2e^2h^2}{3\sqrt{3}c(2\pi m)^{3/2}}\frac{z^3N_ig_{ff}}{(kT)^{1/2}(h\nu)^3}, \tag{19}$$

where the free-free Gaunt factor g_{ff} is taken as unity. Then the total free-free absorption coefficient is

$$\mu_{ff}(h\nu)=\sum_{i} N_i\sigma_{ff}(h\nu). \tag{20}$$

The scattering contribution to the absorption μ_{scatt} is approximated using the Thomson scattering cross section.

The total opacity is related to the absorption coefficient by

$$\rho\kappa(h\nu)=[\mu_{bb}(h\nu)+\mu_{bf}(h\nu)+\mu_{ff}(h\nu)]\times(1-e^{-h\nu/kT})+\mu_{scatt}, \tag{21}$$

where ρ is the density of plasma, and κ is the opacity. In practical applications, Rosseland and Planck mean opacities are usually required, they are defined, respectively, by

$$\frac{1}{K_R}=\int_0^{\infty}\frac{W_R(u)du}{\kappa(u)} \tag{22}$$

and

$$K_P=\int_0^{\infty}[\kappa(u)-\kappa_{scatt}(u)]W_P(u)du, \tag{23}$$

where $u=h\nu/kT$ and κ_{scatt} is the opacity of scattering. W_R and W_P are Rosseland and Planck weighting functions:

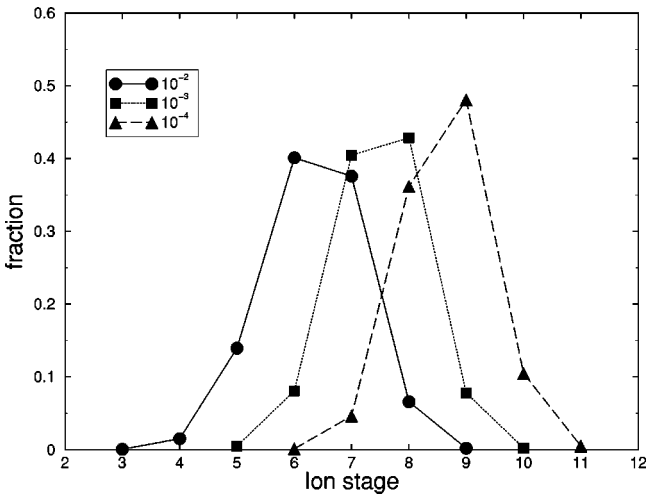

FIG. 1. Populations of different charged ions at a temperature of 20 eV and the densities of 10^{-2}, 10^{-3}, and 10^{-4} g/cm^3. The mean ionization degrees are 6.343, 7.501, and 8.657, respectively.

$$W_R(u)=\frac{15}{4\pi^4}\frac{u^4e^{-u}}{(1-e^{-u})^2} \tag{24}$$

and

$$W_P(u)=\frac{15}{\pi^4}\frac{u^3e^{-u}}{(1-e^{-u})}. \tag{25}$$

In experimental research, people do not measure opacity directly but measure the transmission instead. The relation between opacity and transmission is

$$F(h\nu)=e^{-\rho\kappa(h\nu)L}, \tag{26}$$

where L is the path length traversed by the light through the plasma. The function F is integrated over a Gaussian function with the full width corresponding to the spectrometer resolution to obtain the final transmission spectrum.

III. RESULTS AND DISCUSSION

For the isothermal sequence of $T=20$ eV, we calculated the radiative opacities of iron plasma at the densities of 10^{-2}, 10^{-3} and 10^{-4} g/cm^3. Figure 1 shows the population distributions of ions under different conditions. The mean ionization degrees are 6.34, 7.50, and 8.66, respectively.

Figure 2 illustrates the contributions of bound-bound, bound-free, and free-free absorptions to the total opacity at $T=20$ eV and $\rho=0.01$ g/cm^3. At the photon energy range of 0–300 eV, transitions from K and L shells have no contributions to the spectrum because their transition energies are above 730 eV. So we take K and L shells as the core of the configurations and keep frozen in our calculations. For some iron ions, the $3d$ orbital can be half-filled and may result in a very large set even for the LS coupling. In order to keep the CI expansion in a manageable set, we generate our configurations by a set of reference configurations, in which one electron in the M shells is excited to a higher orbital. The

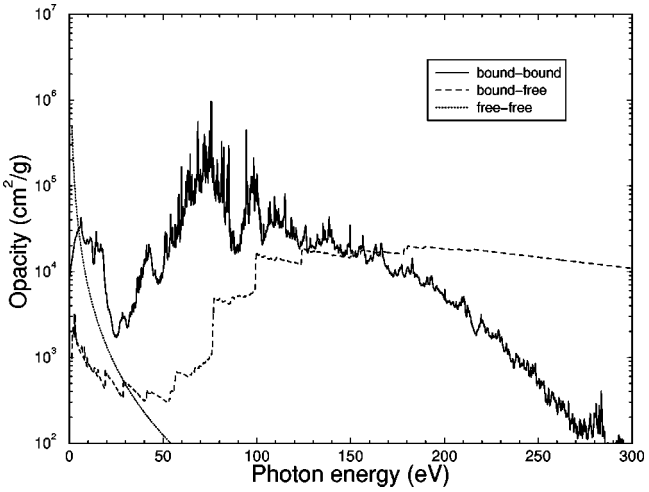

FIG. 2. The bound-bound, bound-free, and free-free opacities at $T=20$ eV and $\rho=0.01$ g/cm^3. The solid line refers to the bound-bound opacity, the dashed line refers to the bound-free opacity, and the dotted line to the free-free opacity.

reference configurations are shown in Table I. For the bound-bound absorption, the peaks are caused by the transitions among the orbitals of M and N shells. Their transition energies are listed in Table II. In the photon energy range of 0–25 eV, the opacities are mainly contributed by the abundant transitions between the nl and $n'l'$ orbitals of high excited states with $n,n'>3$. In the range of 25–47 eV, the absorption peak is caused by the transition from $3s$ to $3p$. From 47 to 89 eV the absorption is dominated by the transitions of $3p \rightarrow 3d$ and $3d \rightarrow 4p$. The peak in the range of 89–103 eV is due to the absorption of $3d \rightarrow 4f$. The opacity above 103 eV is mainly attributed to the transitions from $3s$, $3p$ to nl ($nl \geqslant 4$) orbitals and $3d$ to $n'l'$ ($n'l' \geqslant 5$) orbitals. From Eq. (24) and (25), we know that the Rosseland and Planck weighting functions reach their maxima at 76.6 eV and 58.8 eV, respectively, for a temperature of 20 eV. So the Rosseland and Planck mean opacities are mainly dominated by the

TABLE I. Choices of reference configurations for Fe VII, Fe VIII, Fe IX, Fe X. All configurations have a core of $1s^2 2s^2 2p^6$.

Ion	References
Fe VII	$3s^2 3p^6 3d^2$, $3s^2 3p^6 3dnl$[a], $3s^2 3p^5 3d^3$, $3s^2 3p^5 3d^2 nl$[a], $3s 3p^6 3d^3$, $3s 3p^6 3d^2 nl$[c], $3s^2 3p^4 3d^4$, $3s^2 3p^4 3d^3 nl$[c], $3s^2 3p^3 3d^5$
Fe VIII	$3s^2 3p^6 3d$, $3s^2 3p^6 nl$[a], $3s^2 3p^5 3d^2$, $3s^2 3p^5 3dnl$[b], $3s 3p^6 3dnl$[c], $3s^2 3p^3 3d^4$
Fe IX	$3s^2 3p^6$, $3s^2 3p^5 nl$[a], $3s^2 3p^4 3d^2$, $3s^2 3p^4 3dnl$[c], $3s 3p^5 3d^2$, $3s 3p^5 3dnl$[c], $3s^2 3p^3 3d^3$, $3p^6 3d^2$
Fe X	$3s^2 3p^5$, $3s^2 3p^4 nl$[a], $3s 3p^6$, $3s 3p^5 nl$[c], $3s^2 3p^3 3d^2$, $3s^2 3p^3 3dnl$[c]

[a] $n \leqslant 9, l \leqslant 4$.
[b] $n \leqslant 5, l \leqslant 4$.
[c] $n \leqslant 4, l \leqslant 3$.

TABLE II. Some calculated transitions with their excited energies and weighted oscillator strengths of Fe VII and Fe VIII.

Transition	gf_l	ΔE (eV)
$3s^2 3p^6 3d^2\ ^3F_4$-$3s^2 3p^5 3d^3\ ^3D^o_3$	3.549	71.50
$3s^2 3p^6 3d^2\ ^3F_4$-$3s^2 3p^6 3d4p\ ^3D^o_3$	1.105	53.97
$3s^2 3p^6 3d^2\ ^3F_4$-$3s^2 3p^5 3d^2(^3F)4s\ ^3D^o_3$	0.325	94.73
$3s^2 3p^6 3d^2\ ^3F_4$-$3s^2 3p^6 3d4f\ ^3D^o_3$	0.241	84.77
$3s^2 3p^5 3d^3(^2G)\ ^1G^o_4$-$3s 3p^6 3d^3(^2H)\ ^1H^o_5$	0.479	41.73
$3s^2 3p^6 3d^2\ ^1D_2$-$3s^2 3p^5 3d^3(^2D)\ ^1D^o_2$	1.470	64.40
$3s^2 3p^6 3d^2\ ^1D_2$-$3s^2 3p^6 3d4p\ ^1D^o_2$	0.472	51.00
$3s^2 3p^6 3d^2\ ^1D_2$-$3s^2 3p^5 3d^2(^1D)4s\ ^1D^o_2$	0.544	97.74
$3s^2 3p^5 3d^2(^1G)\ ^2F^o_{7/2}$-$3s 3p^6 3d^2(^3F)\ ^2F_{7/2}$	0.121	40.02
$3s^2 3p^5 3d^2(^3F)\ ^2G^o_{9/2}$-$3s 3p^6 3d^2(^3F)\ ^2F_{7/2}$	0.196	37.35
$3s^2 3p^6 3d\ ^2D_{5/2}$-$3s^2 3p^6 4p\ ^2P^o_{3/2}$	0.682	62.71
$3s^2 3p^6 3d\ ^2D_{5/2}$-$3s^2 3p^6 4f\ ^2F^o_{7/2}$	3.480	94.27
$3s^2 3p^6 3d\ ^2D_{5/2}$-$3s^2 3p^5 3d^2(^3F)\ ^2F^o_{7/2}$	4.424	68.60
$3s^2 3p^6 3d\ ^2D_{5/2}$-$3s^2 3p^5 3d(^3F^o)4s\ ^2F^o_{7/2}$	0.577	106.39

M shell to M shell ($\Delta n=0$) and M shell to N shell transitions.

Since the DCA [19] model does not consider the term splitting of configurations, the photoionization cross section shown in Fig. 2 has no complex line structures such as the bound-bound absorptions but a smooth background with many thresholds. Table III shows the ionization energies of the orbitals of the ground states of Fe VI, Fe VII, and Fe VIII. When the photon energy increases to the ionization threshold of an orbital, the absorption increases immediately and then decreases slowly till the next threshold. The thresholds below 76 eV are caused by the nl ($n>3$) orbitals. Near 76.5 eV, the photon energy reaches the ionization threshold of the $3d_{5/2}$ and $3d_{3/2}$ orbitals of the ground state of Fe VI. This threshold has a slight splitting due to the splitting of $3d_{5/2}$ and $3d_{3/2}$ orbitals, which have the ionization energies of 76.549 eV and 76.352 eV, respectively. At these two thresholds, the opacity of photoionization increases sharply from 1113 cm^2/g to 4880 cm^2/g. The thresholds near 99.3 eV and 123.5 eV belong to the $3d$ orbitals of Fe VII and Fe VIII. After these three thresholds, the absorption of photoionization reaches the same order of the bound-bound absorption. With continuous increase of the photon energy, the $3p$ and $3s$ orbitals are opened sequentially and the photoionization becomes the dominant contribution to the total opacity while the bound-bound absorption decreases quickly. Because the photoionization cross section is small near the maximum of the Planck and Rosseland weighting functions, it has only a

TABLE III. Calculated ionization energies (eV) of the orbitals of the ground states of Fe VI, Fe VII, and Fe VIII.

Ion	$3d_{5/2}$	$3d_{3/2}$	$3p_{3/2}$	$3p_{1/2}$	$3s_{1/2}$
Fe VI	76.352	76.549	130.442	132.155	165.349
Fe VII	99.059	99.279	153.500	155.297	188.751
Fe VIII	123.728	123.972	178.228	180.118	213.801

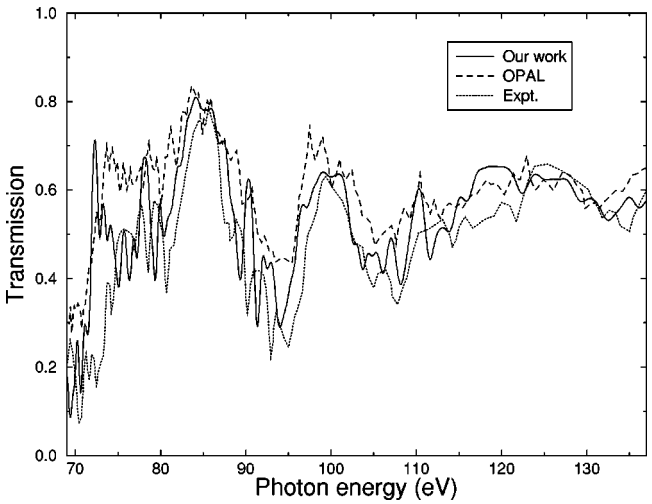

FIG. 3. Comparison of transmissions at a temperature of 22 eV and a density of 0.01 g/cm^3. The solid line refers to the present work, the dotted line refers to the experiment [11], and the dashed line to the result of OPAL [1].

minor contribution to the mean opacities compared with the bound-bound absorption.

The free-free absorption illustrated in Fig. 2 shows us that this part is important only when photon energy is small and plays rather a minor role compared with the other two parts. Figure 5 (a) shows the sum of the bound-bound, bound-free, and free-free opacities of iron opacity at the temperature of 20 eV and the density of 0.01 g/cm^3.

Experiments are extremely important to the development and validation of opacity models. A number of crucial experiments [10–15,24,25] have been performed over the last decade and have served to test, in some manner, virtually all of today's sophisticated opacity codes. First, we have simulated Winhart's experiment [11] for the transmission of iron plasma at a temperature of 22 eV and the density of 0.01 g/cm^3. Figure 3 shows the comparisons among our work, OPAL [1] and the experimental spectrum. From Fig. 3 one can see that in the photon energy range of 70–90 eV, which is mainly dominated by the $3p \rightarrow 3d$ transitions, the absorptions calculated by OPAL are much larger than that of the experiment and ours. OPAL obtained their atomic data by single configuration Hartree-Fock (HF) method while the CI with other configurations was not included. In our calculation we found that the single configuration HF method gave a relatively worse set of energy levels than the MCHF method did, and would overestimate the oscillator strengths especially for the $3p \rightarrow 3d$ transitions from the ground states. Take Fe VIII as an example, Table IV gives the energy levels calculated by MCHF and HF, respectively, as well as the experimental levels [26] for comparison. The same radial wave functions have been used in both methods. In MCHF calculation, we found that the $3p^3$-$3d^3$ and $3p^2$-$3d^2$ electron correlations are very important to the calculation of energy levels and oscillator strengths. Although some lower energy levels calculated by HF method agree better with experiment than by MCHF, the higher levels of HF tend to get higher and higher than that of MCHF, which keeps nearly a constant shift from experiment. Take the $3p^5 3d^2$ configuration as an example, it has a wide energy extension. For some lower states of this configuration, the HF levels are lower than that of MCHF and agree better with the experiment. For examples, the HF energy levels of $3p^5 3d^2(^1G)\ ^2F^o_{5/2}$, $3p^5 3d^2(^1G)\ ^2F^o_{5/2}$, and $3p^5 3d^2(^1D)\ ^2F^o_{7/2}$ are 430 817, 434 367, and 448 676 cm^{-1}, respectively, and in good agreement with the corresponding experimental values of 431 250, 434 555, and 447 656 cm^{-1}. But for higher levels such as $3p^5 3d^2(^3F)\ ^2F^o_{5/2,7/2}$ and $3p^5 3d^2(^3P)\ ^2P^o_{1/2,3/2}$, the HF energies are 562 075, 567 621, 614 741, and 617 587 cm^{-1}, respectively, while the experimental values are 535 909, 541 755, 591 964, and 595 152 cm^{-1} and the corresponding MCHF levels are 550 169, 555 261, 609 560, and 612 548 cm^{-1}. The high MCHF levels behave more like a global shift with experiment. From Table V one can see that the weighted oscillator strengths calculated by single configuration HF method are considerably larger than that calculated by MCHF. So the absorption calculated by MCHF method is much lower than that by HF method. Generally, one believes that the MCHF method can give better energy levels than the HF does. In particular, the oscillator strengths calculated by the MCHF method are much more reliable than those by the HF method.

Although several experimental measurements of iron opacity had been done, lower plasma density and more reliable LTE conditions had not been realized until Springer *et al.* [15] reported their experiment in 1997. They performed a measurement of the x-ray transmission of LTE iron plasma at the conditions of a temperature of 20 eV and a density of 10^{-4} g/cm^3 quite close to the temperature and density in a real astrophysical plasma. For the iron plasma of low densities, the Rosseland mean opacity is sensitive to the treatment of individual lines and then more detailed structures need to be measured. With improved experimental instruments and techniques they obtained a high resolved transmission spectrum. The photon energy ranges from 62.5 eV to 90 eV, which are in the vicinity of the M shell $\Delta n = 0$ bump. The comparison between our result and the experiment is plotted in Fig. 4. An excellent agreement between experimental and theoretical data has been achieved. Our DTA results have convoluted with an instrumental resolving power according to the experiment and have been systematically shifted by 2.7 eV to the lower photon energy to fit the major absorption structures. The spectrum has so many lines that it is unpracticable to accurately calculate all the transition energies. At 82.6 eV and 85.2 eV, both experimental and theoretical spectra have strong absorption, but they are not exactly the same. The experimental absorption at 82.6 eV is much stronger than DTA result while it is reversed at 85.2 eV. The Planck and Rosseland mean opacities are averaged integrations with photon energy, such slight differences can generally be negligible.

Many groups have developed theoretical models and computer codes [1–3] to calculate the iron opacities and published their results of different temperatures and densities. Large disagreement was found among the results when the density was lower than 10^{-3} g/cm^3. Agreement improves as

TABLE IV. Energy levels (in cm^{-1}) of Fe VIII. Experimental data [26] are given for the comparison with the energy levels calculated by the MCHF and HF methods. All configurations have a core of $1s^2 2s^2 2p^6 3s^2$.

Configuration	Term	J	MCHF	HF	Expt.
$3p^6 3d$	^2D	3/2	0.00	0.00	0.00
$3p^6 3d$	^2D	5/2	1934	1833	1836
$3p^5 3d^2(^1G)$	$^2F^o$	5/2	435696	430817	431250
$3p^5 3d^2(^1D)$	$^2D^o$	5/2	436369	430007	
		3/2	439677	431868	
$3p^5 3d^2(^1G)$	$^2F^o$	7/2	439993	434367	434555
$3p^5 3d^2(^1D)$	$^2P^o$	1/2	443121	440416	
		3/2	445953	443374	
$3p^5 3d^2(^1D)$	$^2F^o$	7/2	456069	448676	447656
		5/2	465622	460472	459367
$3p^5 3d^2(^1S)$	$^2P^o$	3/2	519755	519200	508518
		1/2	529111	529054	520822
$3p^5 3d^2(^3F)$	$^2F^o$	5/2	550169	562075	535909
		7/2	555261	567621	541755
$3p^5 3d^2(^3P)$	$^2P^o$	1/2	609560	614741	591964
		3/2	612548	617587	595152
$3p^5 3d^2(^3F)$	$^2D^o$	5/2	610998	628819	596463
		3/2	611250	629102	597065
$3p^6 4f$	$^2F^o$	5/2	762179	772315	763703
		7/2	762291	772361	763799
$3p^5 3d(^3P^o)4s$	$^2P^o$	1/2	840465	846245	837661
		3/2	841460	851326	842829
$3p^5 3d(^3F^o)4s$	$^4F^o$	9/2	849074	852776	
		7/2	852776	855258	847145
		5/2	855660	857899	849899
		3/2	857723	860585	852849
$3p^5 3d(^3F^o)4s$	$^2F^o$	7/2	860029	864845	855100
		5/2	866205	870220	860615

a density of 0.1 g/cm^3 being approached but then tends to degrade a bit at higher densities. We have calculated an isothermal sequence of iron opacities at the temperature of 20 eV with the density ranging from 10^{-4} to 10^{-2} g/cm^3. The results are shown in Fig. 5. From Eq. (13) we see that the Doppler HWHM depends only on the temperature and transition energy. At $T=20$ eV, the typical Doppler HWHM has an order of 10^{-3} eV. The electron impact HWHM calculated by Eq. (14) is mainly determined by the temperature and

TABLE V. Weighted oscillator strengths for the transitions of $3p \rightarrow 3d$ from the ground configuration of Fe VIII. They are calculated by the MCHF and HF methods, respectively. All configurations have a core of $1s^2 2s^2 2p^6 3s^2$.

Transition	MCHF (CI)	HF
$3p^6 3d\ ^2D_{3/2}$-$3p^5 3d^2(^3F)\ ^2F^o_{3/2}$	2.8715	4.9089
$3p^6 3d\ ^2D_{3/2}$-$3p^5 3d^2(^3P)\ ^2P^o_{1/2}$	2.0431	2.6984
$3p^6 3d\ ^2D_{3/2}$-$3p^5 3d^2(^3F)\ ^2D^o_{3/2}$	4.5698	6.0357
$3p^6 3d\ ^2D_{5/2}$-$3p^5 3d^2(^3F)\ ^2F^o_{7/2}$	4.1323	7.0949
$3p^6 3d\ ^2D_{5/2}$-$3p^5 3d^2(^3P)\ ^2P^o_{3/2}$	3.6792	4.8754
$3p^6 3d\ ^2D_{5/2}$-$3p^5 3d^2(^3F)\ ^2D^o_{5/2}$	7.0900	9.3605

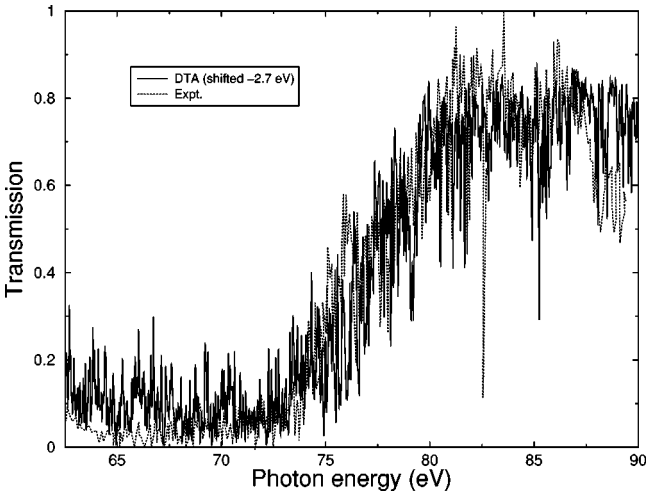

FIG. 4. Comparison between the calculated and experimental [15] transmission of iron plasma at a temperature of 20 eV and a density of 10^{-4} g/cm^3. The dashed line refers to the experiment and the solid line to the theoretical result of DTA.

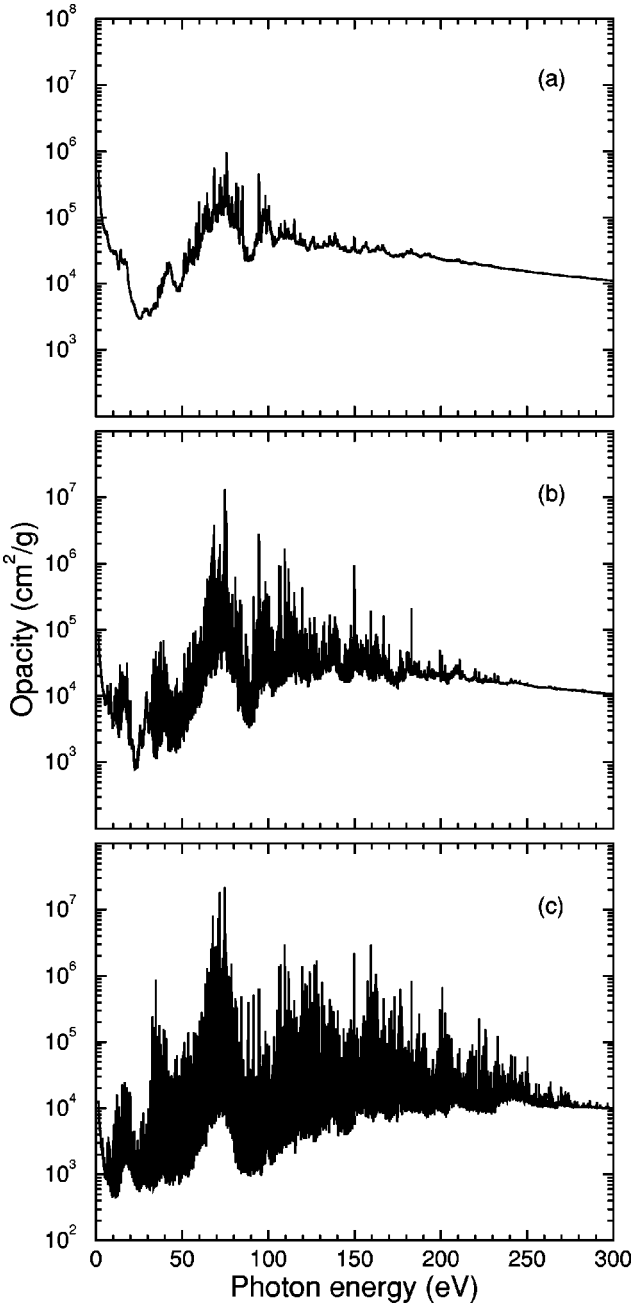

FIG. 5. Spectrally resolved isothermal iron opacities at a temperature of 20 eV and the densities of: (a) $\rho=10^{-2}$ g/cm^3, (b) $\rho=10^{-3}$ g/cm^3, and (c) $\rho=10^{-4}$ g/cm^3. The Rosseland and Planck mean opacities are: (a) $K_r=21283$ and $K_p=56624$ cm$^2/g$, (b) $K_r=8797$ and $K_p=41258$ cm$^2/g$, (c) $K_r=4348$ and $K_p=31185$ cm$^2/g$.

electron density. The typical electron impact HWHMs are 10^{-1} eV at $\rho=10^{-2}$ g/cm^3, 10^{-2} eV at $\rho=10^{-3}$ g/cm^3, and 10^{-3} eV at $\rho=10^{-4}$ g/cm^3. At $\rho=10^{-2}$ g/cm^3, the individual lines near to each other are merged together so that the spectrum shows crude structures. When $\rho \leqslant 10^{-3}$ g/cm^3, the spectra show more details.

From the Eqs. (22) and (23) we know that the Rosseland mean opacity is determined by the depth of the valleys of the spectrum while the Planck mean is determined mainly by the

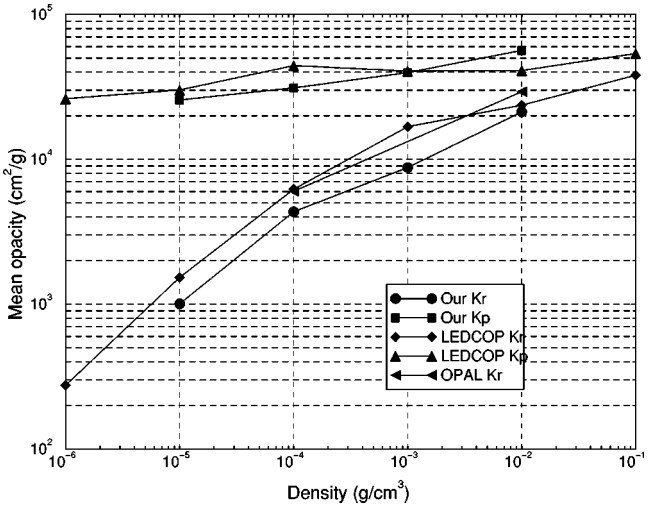

FIG. 6. Comparison of the results among our work, LEDCOP [2], and OPAL [15] for the isothermal Rosseland and Planck mean opacities of the iron plasma at $T=20$ eV.

peaks. The Planck mean opacity is not sensitive to the line shapes and keeps nearly constant when different line profiles are applied. But the situation is different for the Rosseland mean. When the density of the plasma is lower than 10^{-3} g/cm^3, the Rosseland mean opacity strongly depends on the line shapes since in such a case the line wings determine the background of the spectrum. Since many line broadening mechanisms exist in hot plasma, the calculation of line broadening using full quantum theory is so complex and time consuming that it is not applicable for the line by line calculation of opacity. The errors brought by simplified formulas of line width can influence the line wings and the Rosseland mean opacity. The comparisons of our opacities with other results generated by the codes of LEDCOP and OPAL are shown in Fig. 6. At $T=20$ eV, our mean opacities increase at the densities ranging from 10^{-5} to 10^{-2} g/cm^3. For Planck mean opacity, the difference between LEDCOP results and the results in our work is small at the densities of 10^{-5} and 10^{-3} g/cm^3. At 10^{-4} g/cm^3, our result is 31 186 cm$^2/g$, which is 13 193 cm$^2/g$ smaller than that of LEDCOP, but at 10^{-2} g/cm^3, our work is 56 624 cm$^2/g$, which is 15 515 cm$^2/g$ larger than that of LEDCOP. For Rosseland mean opacity, our results are systematically smaller than that of LEDCOP and OPAL. At 10^{-3} g/cm^3, our Rosseland mean opacity is 8797 cm$^2/g$, which is only half of the LEDCOP's value, but at 10^{-2} g/cm^3 our result is 21 283 cm$^2/g$, which is close to the LEDCOP's 23 671 cm$^2/g$. Although all these results are obtained by DTA model, the methods of the calculations of atomic data, level populations and spectral line shapes, and so on are not the same. LEDCOP code obtained most of the atomic energy levels using single configuration LS Hartree-Fock schemes with relativistic corrections. In order to reduce the calculation of the massive atomic data, LEDCOP used an unresolved transition array model for many bound-bound transitions and replaced the actual transition array with a single Gaussian profile to approximate all the actual lines, which would lead to an overestimate for the opacities at low densities. In the present

work, we performed an extensive CI calculation to optimize the atomic levels. For iron, the relativistic effects on energy levels and level splitting are obvious so that the Breit-Pauli relativistic corrections have been included in our calculation. As we have mentioned when discussing the transmissions, the MCHF method gives relatively better energy levels and smaller oscillator strengths compared to the HF method. The transmission spectra just need a 2.7-eV shift toward the lower photon energy in order to fit the main absorption structure of the experiment. Such a spectra shift could cause only little changes in the mean opacities. The uncertainty involved in the line broadening is another important source for the large difference of the Rosseland mean opacities. At $T=20$ eV and $\rho=10^{-4}$ g/cm^3, if we double the Lorentz HWHM, the Rosseland mean opacity will be increased from 4349 to 5201 cm$^2/g$. It is because the increase of linewidth can raise the line wing and then the Rosseland mean opacity.

In summary, we developed a DTA model to calculate the iron opacities. The MCHF method is applied to obtain the bound-bound absorption cross sections. A DCA model is used to calculate the photoionization cross sections and the Kramers approximation is used to evaluate the free-free absorptions. To validate our model, we simulated the experimental transmissions at the conditions of 22 eV, 10^{-2} g/cm^3 and 20 eV, 10^{-4} g/cm^3. In the current work, the multiconfiguration interaction was applied and better energy levels and oscillator strengths were generated resulting in a good agreement between experiment and our theoretical result for the transmission spectrum. Difference still exists between the present and other theoretical models for the mean opacities, and the calculation complexity of the atomic data and line broadening effects are the main sources for these discrepancies.

ACKNOWLEDGMENTS

This work was supported by the National Science Fund for Distinguished Young Scholars under Grant No. 10025416, the National Natural Science Foundation of China under Grants Nos. 19974075 and 10204024, the National High-Tech ICF Committee in China, and the China Research Association of Atomic and Molecular Data.

[1] F.J. Rogers and C.A. Iglesias, Astrophys. J., Suppl. Ser. **79**, 507 (1992).
[2] N.H. Magee, Jr. and R.E.H. Clark, one can get more details of the LEDCOP code of LANL through the web pages at http://www.t4.lanl.gov
[3] F.J.D. Serduke, E. Minguez, Steven J. Davidson, and C.A. Iglesias, J. Quant. Spectrosc. Radiat. Transf. **65**, 527 (2000).
[4] J. Zeng and J. Yuan, Phys. Rev. E **66**, 016401 (2002).
[5] J. Bauche, C. Bauche-Arnoult, and M. Klapisch, Adv. At. Mol. Phys. **22**, 2503 (1987).
[6] A. Bar-Shalom, J. Oreg, M. Klapisch, and T. Lehecka, Phys. Rev. E **59**, 3512 (1999).
[7] J. Yuan, Chin. Phys. Lett. **19**, 1459 (2002).
[8] M.J. Seaton, J. Phys. B **20**, 6363 (1987).
[9] D.G. Hummer, K.A. Berrington, W. Eissner, A.K. Pradhan, H.E. Saraph, and J.A. Tully, Astron. Astrophys. **279**, 298 (1993).
[10] L.B. DaSilva, B.J. MacGowan, D.R. Kania, B.A. Hammel, C.A. Back, E. Hsieh, R. Doyas, C.A. Iglesias, F.J. Rogers, and R.W. Lee, Phys. Rev. Lett. **69**, 438 (1992).
[11] G. Winhart, K. Eidmann, C.A. Iglesias, A. Bar-Shalom, E. Minguez, A. Rickert, and S.J. Rose, J. Quant. Spectrosc. Radiat. Transf. **54**, 437 (1995).
[12] G. Winhart, K. Eidmann, C.A. Iglesias, and A. Bar-Shalom, Phys. Rev. E **53**, R1332 (1996).
[13] P.T. Springer *et al.*, Phys. Rev. Lett. **69**, 3735 (1992).
[14] P.T. Springer *et al.*, J. Quant. Spectrosc. Radiat. Transf. **51**, 371 (1994).
[15] P.T. Springer *et al.*, J. Quant. Spectrosc. Radiat. Transf. **58**, 927 (1997).
[16] C.F. Fischer, Comput. Phys. Commun. **64**, 369 (1991).
[17] C.F. Fischer and P. Jonsson, Comput. Phys. Commun. **84**, 37 (1994).
[18] R.D. Cowan, *The Theory of Atomic Structure and Spectra* (University of California Press, Berkeley, 1981).
[19] S.J. Rose, J. Phys. B **25**, 1667 (1992).
[20] J. Zeng, J. Yuan, and Q. Lu, Phys. Rev. E **64**, 066412 (2001).
[21] J.C. Stewart and K.D. Pyatt, Jr., Astrophys. J. **144**, 1203 (1966).
[22] M.S. dimitrijevic and N. Konjevic, J. Quant. Spectrosc. Radiat. Transf. **24**, 451 (1980).
[23] M.S. dimitrijevic and N. Konjevic, Astron. Astrophys. **172**, 345 (1987).
[24] P.S. Perry *et al.*, Phys. Rev. Lett. **67**, 3784 (1991).
[25] J.M. Foster, D.J. Hoarty, C.C. Smith, P.A. Rosen, S.J. Davidson, S.J. Rose, T.S. Perry, and F.D. Serduke, Phys. Rev. Lett. **67**, 3255 (1991).
[26] C. Corliss and J. Suger, J. Phys. Chem. Ref. Data **11**, 135 (1985).